INVESTIGATION OF FLOW PHENOMENA ON GENERIC DELTA WING

Andrej Furman, Christian Breitsamter
Institute of Aerodynamics, Technische Universität München
Boltzmannstrasse 15, 85748 Garching, Germany

Keywords: *Aerodynamics, Experiments, High Angle of Attack, Vortex Flow, Wind Tunnel*

Abstract

A comprehensive experimental research program on a generic delta wing configuration is conducted as part of the "International Vortex Flow Experiment 2" (VFE–2). The aim of the present study is to set up a validated data base for test of modern CFD codes focusing on methods such as URANS (Unsteady Reynolds Averaged Navier-Stokes) and DES (Detached Eddy Simulation). Flow types of partly developed ($\alpha = 13^o$), fully developed ($\alpha = 18^o$) and burst leading–edge vortices ($\alpha = 23^o$ and $\alpha = 28^o$) are investigated for vortices shed at both sharp and rounded leading edges.

Nomenclature

b	wing span
b_l	local wing span
c_p	pressure coefficient
$\overline{c}_p$	mean pressure coefficient
$\hat{c}_p$	amplitude of pressure coefficient spectrum
c_{prms}	root mean square pressure coefficient
c_r	root chord
d	diameter
d_d	diameter of pressure probe
f	frequency
f_{dom}	dominant frequency
k	reduced frequency
k_{dom}	dominant reduced frequency
l	length
l_μ	mean aerodynamic chord
M_∞	freestream Mach number
p	static pressure
p_∞	freestream static pressure
q	dynamic pressure
q_∞	freestream dynamic pressure
Re_{l_μ}	Reynolds number based on l_μ
r_{LE}	radius of leading edge
s	wing semispan
S_{cp}	power spectrum of pressure coefficient fluctuations
S^N_{cp}	nondimensional power spectrum of pressure coefficient fluctuations
S_p	power spectrum of pressure fluctuations
T	temperature
t	time
t_M	time of measurement
U_∞	freestream velocity
X_p	Fourier transformed quantity of pressure fluctuation
x, y, z	body–axis airfoil coordinates
α	angle of attack
η	fraction of local semispan $\frac{2y}{b_l}$
Λ	aspect ratio
φ	leading–edge sweep
ρ	density

1 Introduction

Delta wing planforms representing lifting surfaces with highly swept leading–edges and low aspect ratios have been investigated intensively over the last 50 years [8]. The dominating flowfield characteristics are given by the evolution

and development of two large–scale vortices shed at the leading-edges. Vortex formation starts already at low angles of attack developing from the rear part to the apex. The shear layer rolls up to form a vortex which is positioned over the wing. This primary vortex is fully developed when vorticity feeding exists over the whole leading–edge. The vortex core shows high axial velocities, low static pressures and increased fluctuations in the subcore area due to the steep gradient in the cross flow components. The leading–edge vortices increase the velocities on the wing upper surface. This velocity increase leads to a high suction level, with the local pressure minima indicating the track of the vortex axis on the wing surface. Therefore, leading–edge vortices in a fully developed, stable stage create additional lift and an increase in maximum angle of attack improving significantly maneuver capabilities of high–agility aircraft.

Delta wing research activities often focus on a sharp leading-edge because primary separation is fixed and the leading–edge vortex development is only little influenced by Reynolds number effects. A blunt leading–edge complicates the vortex aerodynamics as the position of the separation line is free to move determined by the pressure gradient and the boundary layer development. Thus, leading–edge radius, angle of attack and Reynolds number are the main parameters adjusting the onset of vortex evolution as well as position and strength of the primary vortex. For the sharp leading–edge case, the angle of attack is the main parameter only. Considering a chordwise station, the pressure increases from the suction peak induced by the primary vortex to the leading–edge resulting in a severe lateral pressure gradient. Typically, a further separation takes place forming a secondary counter–rotating vortex the evolution of which depends strongly on the presence of a laminar or turbulent boundary layer [9]. Further, leading–edge vortices are subject to breakdown at high angles of attack. Vortex breakdown is caused by the stagnation of the axial core flow due to the increase of the adverse pressure gradient when raising the angle of attack. Therefore, the core expands rapidly accompanied by high velocity fluctuations. The corresponding maxima of fluctuation intensity are located in a limited radial range around the burst vortex core. In addition, the breakdown flow exhibits specific instability mechanisms resulting in narrow–band unsteady aerodynamic forces [1]. The calculation and analysis of such unsteady loads is still a challenging problem which needs the correct representation of the dominating flowfield features.

In the early 1980's Euler methods had reached a development level that an experimental data base was needed for code validation and assessment, especially in the case of leading–edge vortex flow. Therefore, the International Vortex Flow Experiment (VFE–1) has been established carried out in 1984 – 1986. Force and pressure measurements as well as flowfield studies have been performed on a 65^o swept cropped delta wing in several wind tunnel facilities. Results are documented e.g. in [5], [14]. It was shown that even for sharp leading–edges with fixed primary separation there is some lack in accuracy because the Euler code results suffer from the missing secondary separation. In the last ten years great success has been achieved in the development and application of high fidelity computational fluid dynamics methods. Unsteady Reynolds Averaged Navier–Stokes (URANS) Methods are available including a variety of turbulence models based on algebraic up to Reynolds stress transport equations. Also, methods for Detached Eddy Simulations (DES) are formulated as a combination of a Large Eddy Simulation (LES) to model separated flow dominated by large–scale structures in the outer domain and a turbulence model to calculate flow quantities in the wall–bounded domain. Even the upper wing surface pressure distribution is very sensitive to correct modeling viscous effects on the wing as well as in the rolled-up shear layers. Therefore, a second International Vortex Flow Experiment (VFE–2) has been proposed to set up an experimental data base for leading–edge vortex flows including both sharp and blunt leading–edge geometry [10]. Latest experimental techniques should be applied to gather the data fo-

cusing particularly on turbulence and boundary layer quantities. This integrated research activity including partners from Europe and the United States has been started in 2004 and is still on–going.

The present investigation is conducted in frame of the VFE–2 consortium. A generic 65^o swept delta wing configuration [3], [4], [6], [10] is used to study the complex and relevant flow physics in greater detail than it would be possible for a full aircraft configuration. Both sharp and blunt leading–edge cases are addressed.

Up to now, the experiments include steady and unsteady surface pressure measurements and flow visualization using laser light sheet as well as oil flow technique [12], [13]. Steady pressure measurements served as comparison to reference results obtained by NASA [3], [4]. Unsteady pressure measurements inform about vortex bursting when increased pressure fluctuations dominate the breakdown flow. Laser light sheets orientated perpendicular and parallel to the wing surface show the structure and extension of the leading–edge (primary) vortices and to some extent of the secondary vortices. Oil flow visualization is used to study boundary layer development and surface stream lines.

The discussion focuses on the development of the typical vortical flow types as function of angle of attack comparing the effect of rounded vs. sharp leading edge. The flow behaviour on the model is investigated at different angles of attack, especially for partly developed ($\alpha = 13^o$), fully developed ($\alpha = 18^o$) and burst leading–edge vortices ($\alpha = 23^o$ and $\alpha = 28^o$) [7].

2 Experimental and Test Program

2.1 Facility

The measurements have been performed in the large low–speed wind tunnel A of the Institute of Aerodynamics at the Technische Universität München at a Mach number of $M_\infty = 0.07$ and $M_\infty = 0.14$, a Reynolds number based on the mean aerodynamic chord of $Re_{l\mu} = 1 \cdot 10^6$ and $Re_{l\mu} = 2 \cdot 10^6$ and angles of attack varying between $\alpha = 0^o$ and $\alpha = 30^o$. The wind tunnel is of closed–return type with an open test section. The test section is 2.4 *m* in width, 1.8 *m* in height and 4.8 *m* long. The freestream turbulence intensity is less than 0.4%. The uncertainty in the temporal and spatial mean velocity distribution is less than 0.6%. The uncertainty in freestream direction is below 0.2^o and static pressure variations are below 0.4%.

2.2 Model

A generic delta wing model was designed, to study leading–edge vortex flow features comparing the influence of sharp and rounded leading edges. The present model has a root chord length of $c_r = 0.980$ *m*, a wing span of $b = 0.914$ *m*, a leading edge sweep of $\varphi_{LE} = 65^o$, a wing area of $S = 0.448$ m^2 and an aspect ratio of $\Lambda = 1.865$ (Tab. 1) and (Fig. 1).

root chord	c_r	0.980 *m*
wing span	$b = 2s$	0.914 *m*
wing area	F	0.448 m^2
mean aerodynamic chord	l_μ	$2/3c_r$
aspect ratio	Λ	1.865
leading edge sweep angle	φ	65^o

Table 1 Model data.

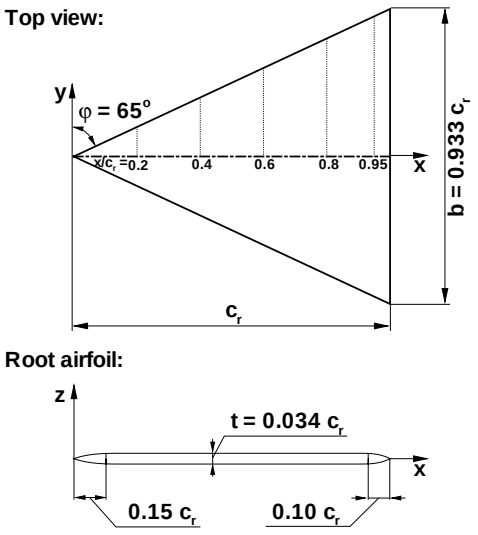

Fig. 1 Geometry of the delta wing model.

The delta wing consists of an upper and a lower base plate, the trailing edge with a depth of $x_{TE}/c_r = 10\%$ and the pressure orifices being part of these plates. On the inside of these plates cut–outs are milled to house the tubes and wires from the pressure orifices and unsteady pressure transducers, respectively. The thickness of the model is $t = 0.033\ m$, which is constant over the base plate. A sharp and a rounded leading edge ($r_{LE,rounded}/l_\mu = 0.0015$) are available, r_{LE} being the leading edge radius and l_μ the mean aerodynamic chord (Fig. 2).

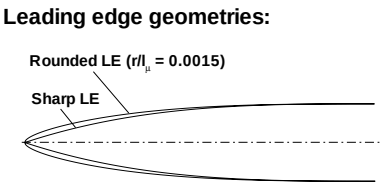

Fig. 2 Comparison of leading edge shape.

The leading edges are fitted on the left and right hand side of the lower base plate and have a depth of $x_{LE}/c_r = 15\%$. Sharp and rounded leading–edge parts are exchangeable. On each of the leading edge elements, five pockets for the pressure sensors have been milled, which are closed with separate lids.

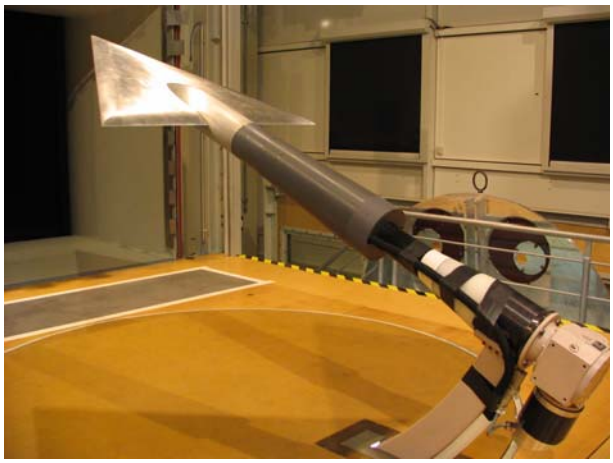

Fig. 3 Delta wing model mounted in test section of wind tunnel facility A.

On the mounted wing a model sting is installed, which is attached to the three–axis model support via a model adapter (Fig. 3). There are 177 pressure orifices with a diameter of $d_d = 0.3\ mm$ situated on the entire wing, of which 44 are equipped with unsteady pressure sensors. The pressure orifices are positioned in five chordwise positions ($x/c_r = 0.2$, 0.4, 0.6, 0.8 and 0.95).

2.3 Steady and Unsteady Surface Pressure Measurements

The steady pressures are measured on the upper– and lower surface of the wing at five chord stations ($x = const.$) with altogether 133 measuring points by means of a Scanivalve. There, the pressure signal is converted into an electrical signal. The sensor queries one orifice after the other, while all others are closed. The scanning rate of the measured values is $f = 100\ Hz$ with an averaging time of $t = 10\ s$ and a settling time of $t = 3\ s$ after each orifice. In this way 48 pressure measuring points per pressure unit are queried after each other. The measurement was accomplished with a Scanivalve with three pressure units, so that a maximum of 144 pressure measuring points could be scanned.

For the unsteady pressure measurements it is necessary to ensure a high scanning rate and measuring accuracy of the pressure sensor. A crucial factor of the measuring accuracy is the distance of the pressure sensor to the measuring point. Therefore, the unsteady pressure sensors are inserted as close as possible to the measuring point, in order to avoid an amplitude– and phase shift. The inserted unsteady pressure sensors of the type Kulite XCS–093–0.35BAR D are equipped with an ambient pressure connection as reference pressure and the peak value of the scanning rate is 300 kHz. The unsteady pressure measurements were accomplished in four chord stations on the suction side of the wing with 12 unsteady pressure sensors per chord station with a scanning rate of $f = 2000\ Hz$ and an averaging time of $t = 40\ s$. The frequency of the analog low–pass filter was set to 256 Hz. The electrical signals of the pressure sensors were recorded

and amplified by the WDV–Measuring system, which was especially developed for this purpose. The signal was then passed on to the measuring computer for evaluation. The resolution of the pressure signal is at a medium sensitivity of 245 mV/bar and a signal amplification of 100 approx. 0.5 Pa, which is highly sufficient for the intended measurements [2].

2.4 Laser Light Sheet Visualisation

This measuring method is used in order to visualise the flow field in a plane, which is illuminated by a laser beam expanded by a cylindrical lense. The smoke particals in this plane are then recorded with a digital photo or video camera. The particle size is approx. 2 μm, in order to guarantee sufficient light reflection. By optimizing the concentration of the smoke above the model, high quality images are achieved. If the concentration is too low, the flow structure will not be fully visible on the image. A concentration which is too high will cause the flow details to vanish. The investigations were conducted at a freestream velocity of $U_\infty = 12\ m/s$, a Reynolds number of $Re_{l\mu} = 5 \cdot 10^5$ and at angles of attack of $\alpha = 0^o \div 30^o$.

For this investigation an air cooled class 3B Argon-Ion-laser was used. This laser has a maximum power of 100 mW and the wave length of the light is between $457 \div 514\ nm$.

A digital photo camera positioned 1350 mm behind the wing's trailing edge was used to record the images. As the camera always needs to be perpendicular to the illuminated light sheet, it was mounted on to the model support and is therefore moved with the angle of attack. In order to be also able to provide pictures from above the model, a circular rail was built, which is 2000 mm above the wing. By moving the camera on the rail, the images are always perpendicular to the wing surface and the light sheet.

2.5 Oil Flow Visualisation

Surface stream lines were photographed on the suction side of the wing at different angles of attack between $\alpha = 0^o \div 30^o$ at freestream velocities of $U_\infty = 12\ m/s, 24\ m/s$ and $48\ m/s$ with the corresponding Reynolds numbers being $Re_{l\mu} = 5 \cdot 10^5, Re_{l\mu} = 1 \cdot 10^6$ and $Re_{l\mu} = 2 \cdot 10^6$. The model was used with both its polished aluminium surface and a stuck–on black foil for this investigation. A mixture of paint pigments, petrol and paraffin was applied on the upper surface and exposed to the freestream flow briefly. The developed flow picture was then photographed.

3 Analysis of Results

3.1 Preparatory Tests

First of all the quality of the measurements were judged by comparison with the steady pressure measurements obtained by NASA [3], [4]. Fig. 4 and Fig. 5 illustrates the comparison between NASA results at $Re_{l\mu} = 2 \cdot 10^6$, $M_\infty = 0.2$ and the results obtained by Technische Universität München at $Re_{l\mu} = 2 \cdot 10^6$, $M_\infty = 0.14$. The comparison shows an excellent agreement between the steady pressure distribution, which clearly illustrates the comparability in terms of freestream, wind tunnel and model conditions.

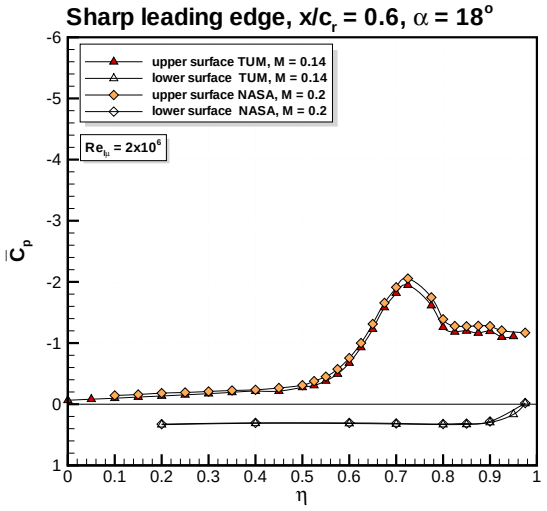

Fig. 4 Comparison between NASA– and TUM–measurements for sharp leading edge at $Re_{l\mu} = 2 \cdot 10^6$ and $\alpha = 18^o$

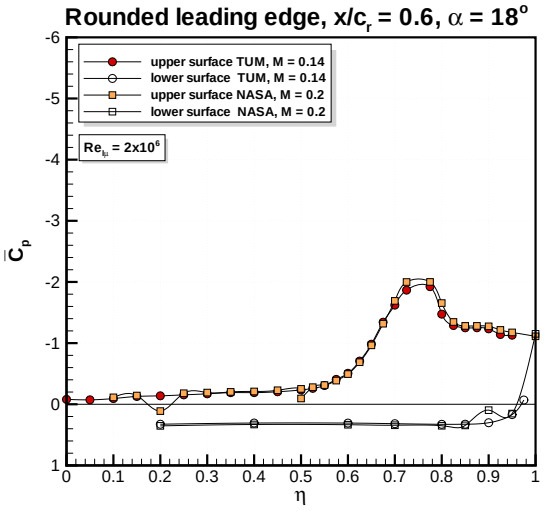

Fig. 5 Comparison between NASA– and TUM–measurements for rounded leading edge at $Re_{l\mu} = 2 \cdot 10^6$ and $\alpha = 18^o$

3.2 Steady Pressure and Pressure Fluctuation Intensity

The discussion of the results is done by the time–averaged pressure coefficients and the intensity of the pressure fluctuations [1], [2].

For the time–averaged and rms–pressure coefficients the surface pressures $p(P,t)$ at the position P are converted in non dimensional values. The pressure coefficient is defined by

$$c_p(P,t) = \frac{p(P,t) - p_\infty}{q_\infty} \tag{1}$$

where $p(P,t)$ is the static pressure, p_∞ the static freestream pressure and q_∞ the dynamic pressure. For each position P on the upper wing surface the time series of the non dimensional pressure coefficient $c_p(P,t)$ are then available at every test condition.

The average of the pressure coefficient $\overline{c}_p(P,t)$ is defined as

$$\overline{c}_p(P) = \frac{1}{t_M} \int_0^{t_M} c_p(P,t)\, dt \tag{2}$$

where t_M is the time of measurement or the length of the time series. The fluctuation part of the pressure coefficient $c'_p(P,t)$ is described by

$$c'_p(P,t) = c_p(P,t) - \overline{c}_p(P). \tag{3}$$

The mean square value of the pressure coefficient $\overline{c'^2_p}(P)$ is therefore

$$\overline{c'^2_p}(P) = \frac{1}{t_M} \int_0^{t_M} [c_p(P,t) - \overline{c}_p(P)]^2\, dt. \tag{4}$$

The root of the mean square value is denoted rms–value $c_{p_{rms}}(P)$:

$$c_{p_{rms}}(P) = \sqrt{\overline{c'^2_p}(P)} \tag{5}$$

Three angles of attack were chosen for a detailed analysis, namely $\alpha = 13^o$, $\alpha = 18^o$ and $\alpha = 23^o$. At an angle of attack of $\alpha = 13^o$, the primary vortex is not yet fully developed, at $\alpha = 18^o$ the primary vortex is fully developed, whereas at an angle of attack of $\alpha = 23^o$ the primary vortex breaks down over the wing [7].

For the case with the sharp leading edge the separation line of the primary vortex is fixed at the sharp leading edge and, therefore, no significant influence of the Reynolds number is noticeable. The separation on the rounded leading edge is a far more complex phenomenon, as the primary separation is not defined by a geometric discontinuity as for the sharp leading edge (Fig. 6). For this reason the separation as well as the vortex development is dependent on the freestream flow and the geometry of the leading edge.

At low to medium angles of attack the flow is still fully attached for the rounded leading edge. The separation of the leading edge vortex occurs at the rear part of the leading edge and moves towards the apex with increasing angle of attack. Therefore, the wing shows a partially developed separation at the leading edge, whereas the upstream part of the wing still shows attached flow. On the downstream part of the wing a leading edge vortex forms. The separation line can

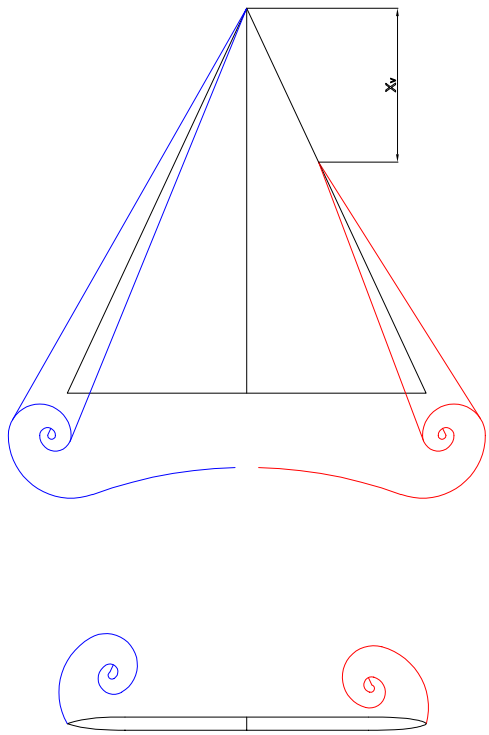

Fig. 6 Leading edge radius effect on primary vortex structure.

move freely on the leading edge, depending on Reynolds and Mach number as well as on the leading edge radius [8], [9], [11].

At an angle of attack of $\alpha = 13^o$ (Fig. 7), the suction peaks on the upper surface of the wing are clearly visible. These suction peaks decrease downstream, except between the chord stations $x/c_r = 0.2$ and $x/c_r = 0.4$, where the suction peak at $x/c_r = 0.4$ is higher due to a not yet fully developed vortex. The constant pressure level at the inner wing indicates reattached flow. The secondary separation is also noticeable as an increased suction level near the leading edge, except for the chord station $x/c_r = 0.2$. Further downstream, the suction peaks moves more to the center portion of the wing and the vortex turns from the leading edge towards the freestream flow direction.

Increasing the angle of attack to $\alpha = 18^o$ (Fig. 8), the suction peaks also increase, according to the stronger vortex indicated for all chord stations. The increase in vortex diameter corresponds to the broadened areas of suction and moves the reattachment line further towards the wing center.

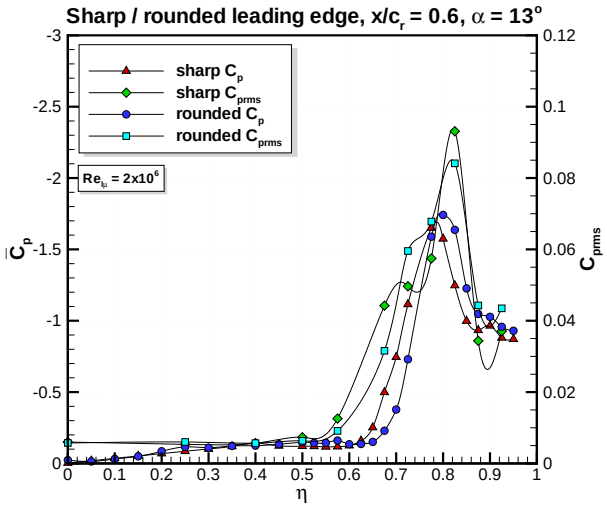

Fig. 7 Steady pressure distribution and pressure fluctuation intensity for sharp and rounded leading edges at $\alpha = 13^o$.

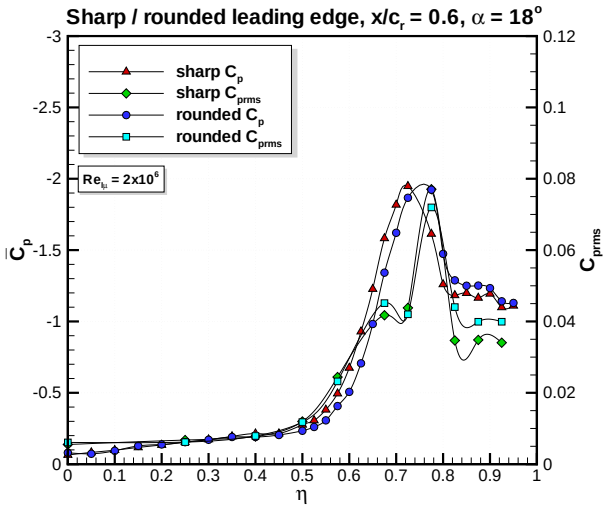

Fig. 8 Steady pressure distribution and pressure fluctuation intensity for sharp and rounded leading edges at $\alpha = 18^o$.

Further increasing the angle of attack to $\alpha = 23^o$ (Fig. 9), increases the suction peaks at the chord stations $x/c_r = 0.2$, 0.4 and 0.6 for both the sharp and the rounded leading edges and at $x/c_r = 0.8$ for the rounded leading edge.

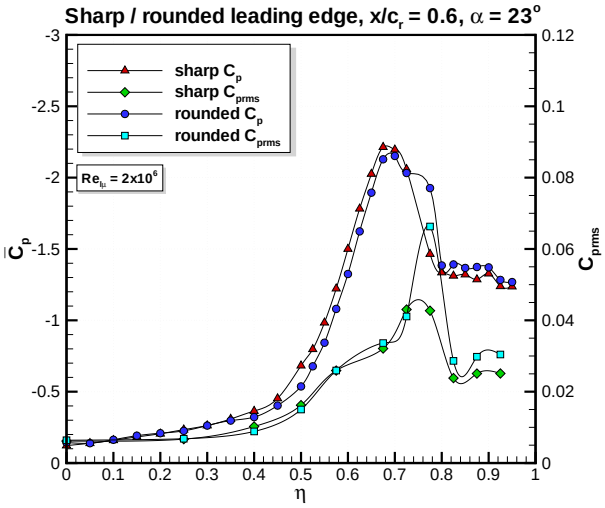

Fig. 9 Steady pressure distribution and pressure fluctuation intensity for sharp and rounded leading edges at $\alpha = 23^o$.

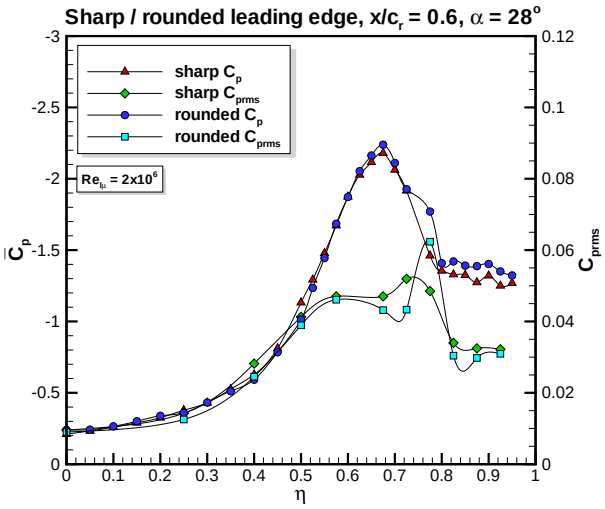

Fig. 10 Steady pressure distribution and pressure fluctuation intensity for sharp and rounded leading edges at $\alpha = 28^o$.

The position of the breakdown point is determined by the pressure distribution. If the increase in angle of attack does not cause an increased suction peak, then the leading edge vortex has broken down in a plane at $x/c_r = const$. This criteria fails, if the primary vortex detaches from the wing surface and thereby reduces its influence on the pressure distribution at the same time, as the breakdown point passes the trailing edge upstream. The detachment of the vortex axis for strong leading edge vortices as for this delta wing, with a leading edge sweep of $\varphi = 65^o$, is only observed at angles of attack beyond the ones investigated here. Therefore, the described breakdown criteria is applicable here.

At $\alpha = 18^o$ and $x/c_r = 0.8$ the pressure coefficient for the suction peak for the sharp leading edge is $c_{p,sharp,0.80} = -1.51$ and for the rounded leading edge at $x/c_r = 0.95$ $c_{p,round,0.95} = -1.06$. With increasing angle of attack the suction peaks are reduced at the rear portion of the wing. Therefore, $c_{p,sharp,0.80} = -1.45$ for $\alpha = 23^o$ and $c_{p,round,0.95} = -0.87$. Therewith, the breakdown point for the primary vortex for the sharp leading edge was determined at $x/c_r = 0.68$ and for the rounded leading edge at $x/c_r = 0.85$. With increasing the angle of attack to $\alpha = 28^o$ (Fig. 10), the breakdown point is rapidly shifted upstream. The position of the breakdown point was verified by the results obtained from the flow field visualisation using smoke and the surface streamline visualisation using oil.

The intensity of the pressure fluctuations shows high values in the vortex region already for low angles of attack. However, the highest fluctuations are shifted towards the leading edge in comparison with the suction peak. For the rounded leading edge the highest *rms* values occur at an angle of attack of $\alpha = 13^o$ at $x/c_r = 0.4$ closer to the leading edge as those for the sharp leading edge. With increasing chord station as well as with increasing angle of attack the positions of the highest pressure fluctuations approach each other. The *rms* levels increase with increasing angle of attack up to $\alpha = 21^o$ reaching a maximum of $c_{prms} = 0.118$ for the sharp leading edge. For the rounded leading edge this

trend is up to $\alpha = 18^o$ with a maximum of $c_{prms} = 0.135$ at $x/c_r = 0.4$. Thereafter, the pressure fluctuations decrease to $c_{prms} = 0.075$ at $\alpha = 27^o$ for the sharp leading edge and approx. $c_{prms} = 0.077$ at $\alpha = 29^o$ for the rounded leading edge, until vortex breakdown becomes dominant and the pressure fluctuations increase further. Moving downstream the pressure fluctuation intensity decreases. For the sharp leading edge the maximum is $c_{prms} = 0.075$ at $x/c_r = 0.95$ for an angle of attack of $\alpha = 13^o$ and for the rounded leading edge the maximum is $c_{prms} = 0.119$ at $\alpha = 5^o$.

3.3 Spectral Analysis

Spectral analysis is applied to the values of one channel per measuring plane to study the characteristics in the area of the highest pressure fluctuation intensity.

The fluctuation part $p'(P,t)$ and $p'(\tilde{P},t)$ of the discrete time function $p(P,t)$ and $p(\tilde{P},t)$, respectively is Fourier transformed based on the relation

$$X_p(P,\omega) = \lim_{t_M \to \infty} \int_0^{t_M} p'(P,t)\, e^{-i\omega t}\, dt. \qquad (6)$$

The multiplication of the Fourier transformed quantity $X_p(P,\omega)$ or $X_p(\tilde{P},\omega)$ with its conjugated complex quantities $X_p^*(P,\omega)$ or $X_p^*(\tilde{P},\omega)$ leads to the power spectral density function.

$$S_p(P,\omega) = \lim_{t_M \to \infty} \frac{2}{t_M} X_p^*(P,\omega)\, X_p^T(P,\omega) \qquad (7)$$

$$S_p(P,\tilde{P},\omega) = \lim_{t_M \to \infty} \frac{2}{t_M} X_p^*(P,\omega)\, X_p^T(\tilde{P},\omega) \qquad (8)$$

Accordingly, the power spectral density for the fluctuating part $S_{c_p}(P,\omega)$ can be derived. The power spectral density of the pressure coefficient fluctuations still has the dimension of time. Taking into account the definition of the reduced frequency (Eq. 10) leads to the non dimensional power spectral density of the pressure coefficient fluctuations:

$$S_{c_p}^N(P,k) = \frac{U_\infty}{l_\mu} S_{c_p}(P,k) \qquad (9)$$

$$k = \frac{f l_\mu}{U_\infty} \qquad (10)$$

The non dimensional power spectral density of the pressure coefficient $S_{c_p}^N(P,k)$ can be transformed to an amplitude spectrum of the pressure coefficient:

$$\hat{c}_p(P,k) = \sqrt{2\, S_{c_p}^N(P,k)\, \Delta k} \qquad (11)$$

At an angle of attack of $\alpha = 13^o$ (Fig. 11), the amplitude level of pressure spectra for the rounded leading edge is slightly higher as for the sharp leading edge, especially in the low frequency domain. By increasing the angle of attack to $\alpha = 18^o$ (Fig. 12, Fig. 13, Fig. 14 and Fig. 15), no significant change is noticeable, except for the amplitude spectrum at $x/c_r = 0.4$ for the rounded leading edge. There, the level of the highest frequencies is clearly increased and reaches a maximum $\hat{c}_p = 0.012$ in the area of $k = 2 \div 3.1$, which illustrates the separation of the secondary vortex.

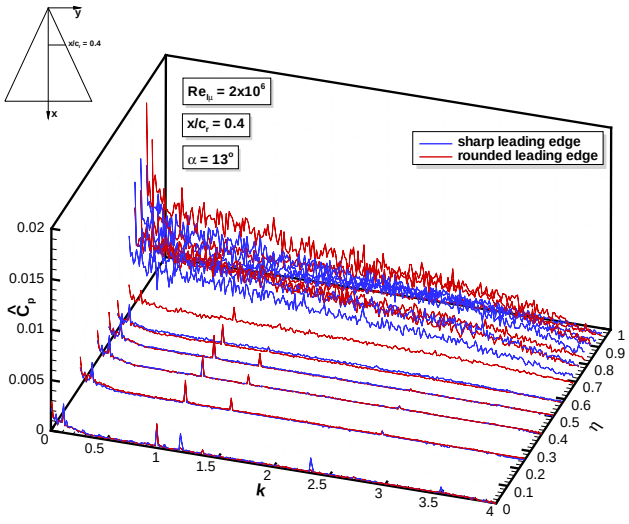

Fig. 11 Amplitude spectra of fluctuating pressure coefficient for sharp and rounded leading edge at $\alpha = 13^o$, $x/c_r = 0.4$, $Re_{l_\mu} = 2 \cdot 10^6$ and $M = 0.14$.

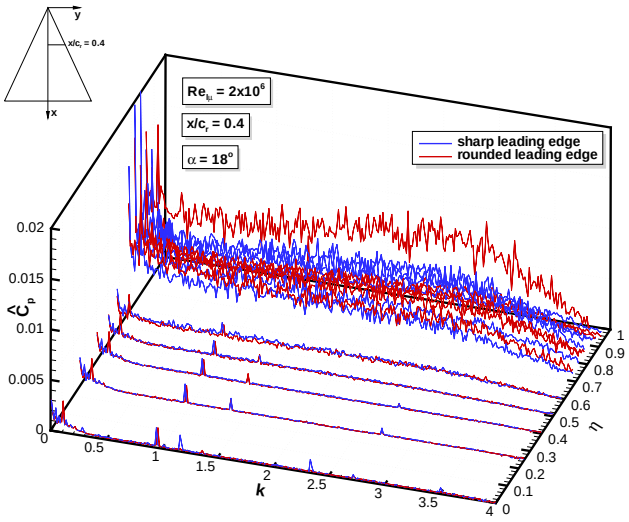

Fig. 12 Amplitude spectra of fluctuating pressure coefficient for sharp and rounded leading edge at $\alpha = 18^o$, $x/c_r = 0.4$, $Re_{l\mu} = 2 \cdot 10^6$ and $M = 0.14$.

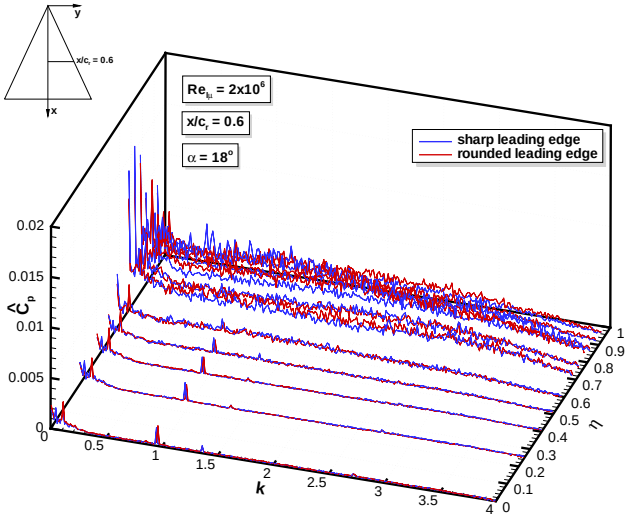

Fig. 13 Amplitude spectra of fluctuating pressure coefficient for sharp and rounded leading edge at $\alpha = 18^o$, $x/c_r = 0.6$, $Re_{l\mu} = 2 \cdot 10^6$ and $M = 0.14$.

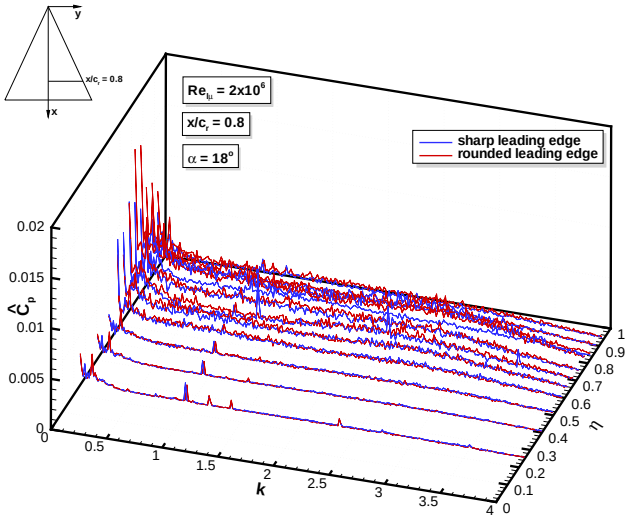

Fig. 14 Amplitude spectra of fluctuating pressure coefficient for sharp and rounded leading edge at $\alpha = 18^o$, $x/c_r = 0.8$, $Re_{l\mu} = 2 \cdot 10^6$ and $M = 0.14$.

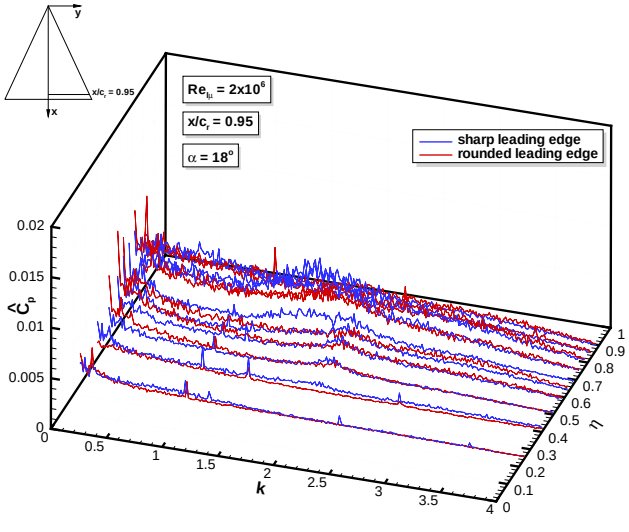

Fig. 15 Amplitude spectra of fluctuating pressure coefficient for sharp and rounded leading edge at $\alpha = 18^o$, $x/c_r = 0.95$, $Re_{l\mu} = 2 \cdot 10^6$ and $M = 0.14$.

At an angle of attack of $\alpha = 23^o$, the increase in amplitude for both leading edge geometries is visible, whereby the increase in the chord station $x/c_r = 0.4$ for the sharp leading edge is more significant. The increase in the chord station $x/c_r = 0.95$ (Fig. 16), especially the amplitude peaks $\hat{c}_p = 0.0095$ at $k = 1.1 \div 1.4$, indicate the breakdown of the primary vortex for both leading edge geometries. Further increasing the angle of attack to $\alpha = 28^o$ (Fig. 17) the area of a narrow–band concentration of turbulent energy is broadened to $k = 0.8 \div 1.4$ and increases to $\hat{c}_p = 0.01$ for both leading edge geometries. This takes place for the rounded leading at $2y/b_l = 0.775$ and for the sharp leading edge at $2y/b_l = 0.825$. An additional increase in the high frequency domain ($k = 2.5 \div 3.0$) to $\hat{c}_p = 0.005$ illustrates the separation at the trailing edge. With the equation

$$k_{dom} = \frac{f_{dom}\, x\, cot\varphi_W}{U_\infty} sin\alpha \qquad (12)$$

a scaled dominant reduced frequency in the frequency range 0.28 ± 0.05 can be determined, as derived in [2] for other delta wing geometries.

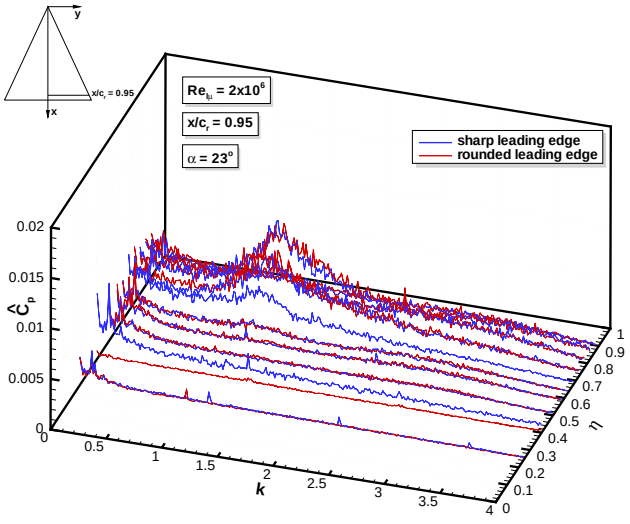

Fig. 16 Amplitude spectra of fluctuating pressure coefficient for sharp and rounded leading edge at $\alpha = 23^o$, $x/c_r = 0.95$, $Re_{l\mu} = 2 \cdot 10^6$ and $M = 0.14$.

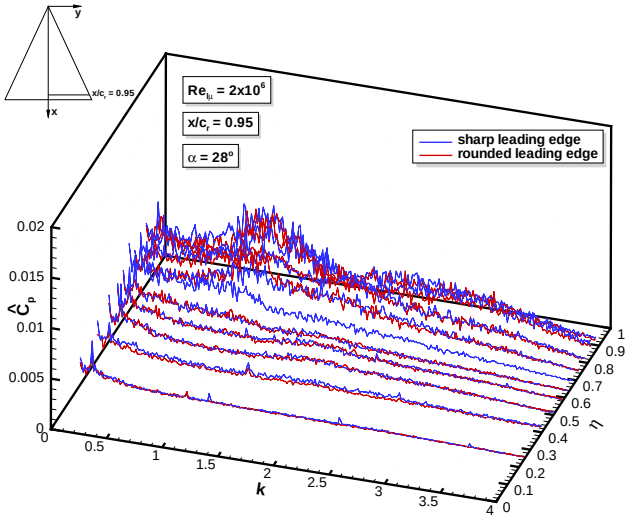

Fig. 17 Amplitude spectra of fluctuating pressure coefficient for sharp and rounded leading edge at $\alpha = 28^o$, $x/c_r = 0.95$, $Re_{l\mu} = 2 \cdot 10^6$ and $M = 0.14$.

3.4 Flow Field

Laser light sheet visualisation can be used to determine the flow behaviour over and behind the wing as well as the size and position of the vortices. The pictures taken from behind the wing in the chord stations $x/c_r = 0.2$, 0.4, 0.6, 0.8, 0.95 and 1.1 are shown on the right hand side of the figures and illustrate a cross section of the vortex. The vortex structure can be illustrated schematically as shown in Fig. 18. The leading edge vortex can be divided into several regions:

- Free shear layer: the free shear layer on the outer surface of the vortex is rolled up and feeds the vortex with circulation.
- Rotational core: the region in which the shear layer is rolled up helically is denoted rotational core. This region fluctuates during the measurements by 20% of the local half span.
- Sub core: the inner, viscous dominated core is surrounded by the rotational core. The measurements showed a size of approx. 10% of the local half span.

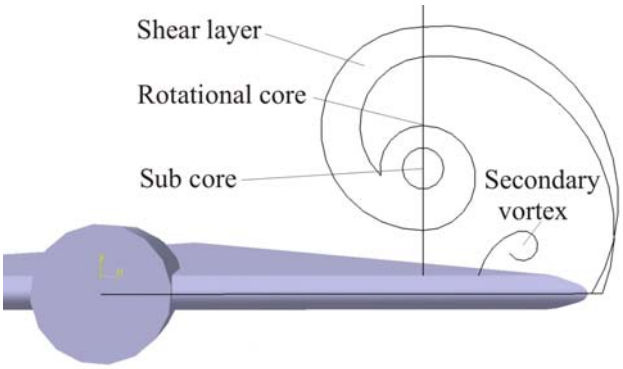

Fig. 18 Schematic illustration of vortex structure.

On the left hand side of the figures the pictures from above, i.e. parallel to the wing upper surface, at $z/c_r = 0.01$ and 0.05 are shown. With these images the position of the leading edge vortex and the breakdown location at high angles of attack can be determined.

The comparison between the sharp and the rounded leading edge shows a delayed separation for the rounded leading edge, which is also indicated by the smaller vortex core and a stronger trailing edge effect (Fig. 19).

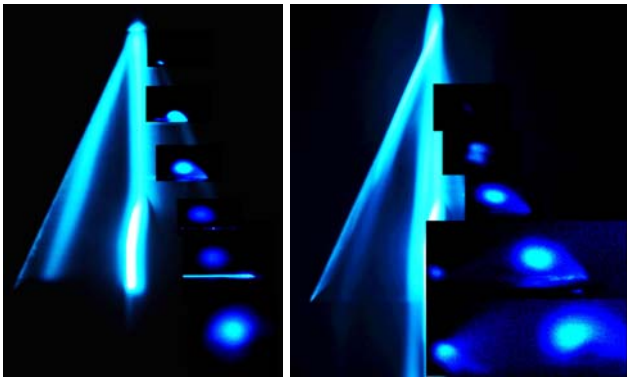

a) sharp leading edge b) rounded leading edge

Fig. 19 Vortex structure above and behind the wing at $\alpha = 13^o$, $Re_{l\mu} = 5 \cdot 10^5$ and $M = 0.035$.

At higher angles of attack (Fig. 20), the vortex cores are larger and positioned closer to the wing center, turning towards the free stream flow direction.

At $\alpha = 23^o$ (Fig. 21), the vortices are quite large in their cross section, especially in the rear area, where the vortices are already bursted.

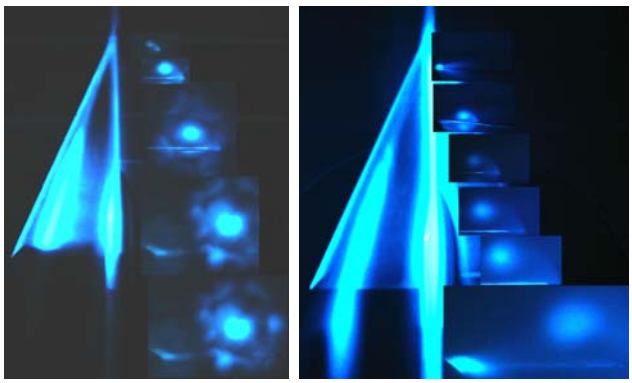

a) sharp leading edge b) rounded leading edge

Fig. 20 Vortex structure above and behind the wing at $\alpha = 18^o$, $Re_{l\mu} = 5 \cdot 10^5$ and $M = 0.035$.

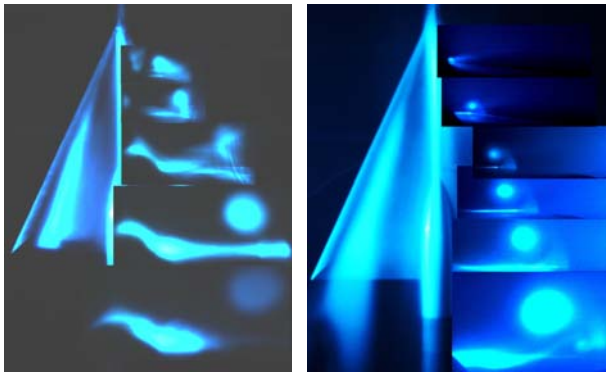

a) sharp leading edge b) rounded leading edge

Fig. 21 Vortex structure above and behind the wing at $\alpha = 23^o$, $Re_{l\mu} = 5 \cdot 10^5$ and $M = 0.035$.

In order to compare the position of the vortex the axis location is investigated. Its position is determined with the images obtained by the use of smoke. The angle $\overline{\varphi}_{VA}$ indicates the lateral position of the axis. As a reference value the angle between the leading edge and the symmetry line $\overline{\varphi}_W$ is used. Fig. 22 and Fig. 23 illustrate the results for both sharp and rounded leading edges. It is shown, that the vortex axis for the rounded leading edge is significantly further inboard as for the sharp leading edge.

Comparing the height of the vortex shows no significant difference up to an angle of attack of $\alpha = 25^o$. There the height of the vortex position for the sharp leading edge increases significantly

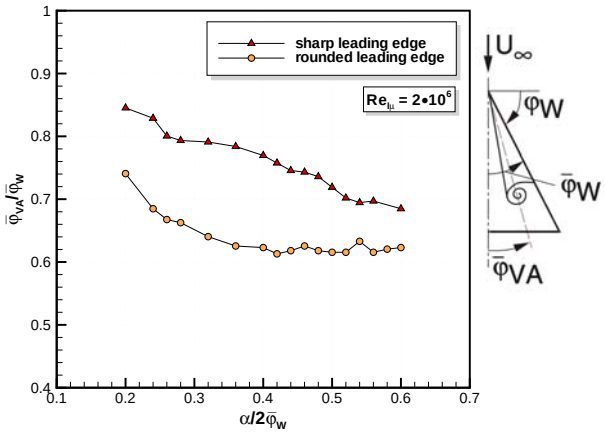

Fig. 22 Lateral position of the vortex axis.

in comparison to the rounded leading edge.

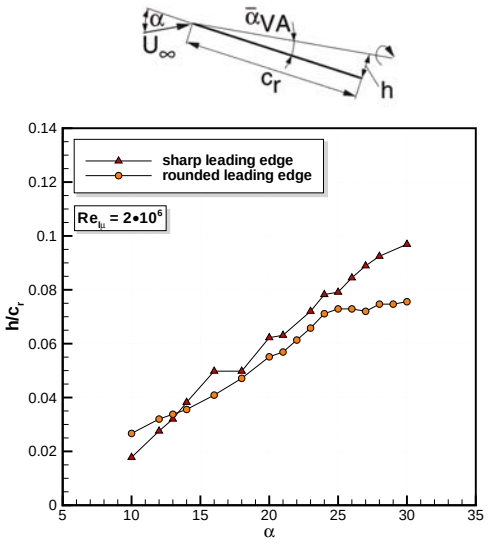

Fig. 23 Height of the vortex axis over the wing.

3.5 Surface Streamlines

The flow turns around the rounded leading edge with high velocity due to the pressure difference between the upper and lower surface of the wing. As the radius of curvature decreases the pressure rises on the upper surface, thus causing a boundary layer separation. Due to the roll up of the shear layer along the leading edge, the leading edge vortex is formed. The line at which the flow coming from below turns around the leading edge and the vortex in order to reattach on the wing upper surface is called reattachment line of the primary vortex (Fig. 24). Between the suction peak of the primary vortex and the leading edge, a strong positive pressure gradient exists, causing a further separation of the boundary layer, which then rolls up into the secondary vortex. The secondary vortex is counter rotating to the primary vortex and the separation and reattachment line can also be detected by the oil flow measurements.

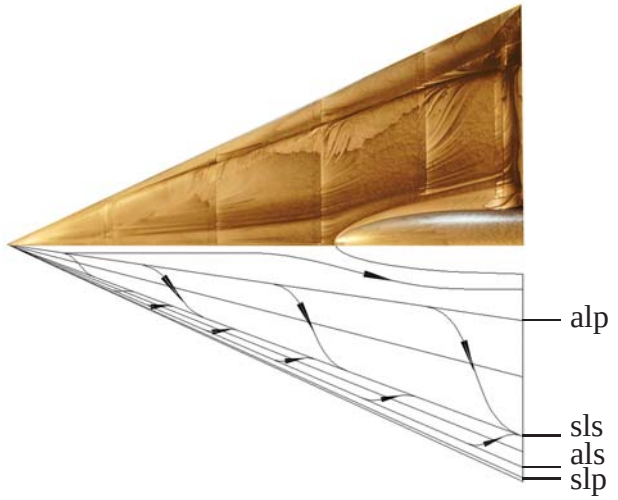

Fig. 24 Surface streamline topology over the wing for rounded leading edge; slp $\sim$ primary vortex separation line, alp $\sim$ primary vortex attachment line, sls $\sim$ secondary vortex separation line, als $\sim$ primary vortex attachment line.

Fig. 25 illustrates the surface stream lines on the suction side of the wing at $\alpha = 13^o$. The location of the primary and secondary vortex can be judged with the help of the primary reattachment line and the secondary separation line. Below the vortex core the highest cross flow velocities can be found. There, the surface stream lines turns towards the leading edge, orientated in cross flow direction.

With increasing angle of attack $\alpha = 18^o$ (Fig.

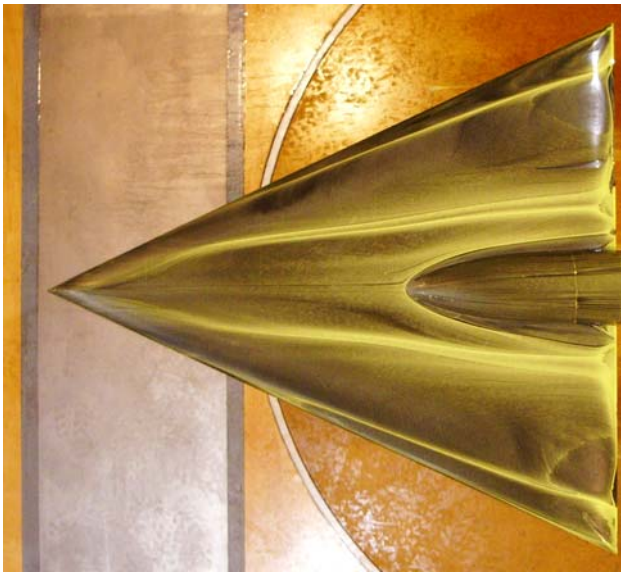

Fig. 25 Streamline visualisation using oil for rounded leading edge at $\alpha = 13^o$, $Re_{l_\mu} = 2 \cdot 10^6$ and $M = 0.14$.

26) the reattachment line of the primary vortex and the separation line of the secondary vortex move towards the symmetry line of the wing.

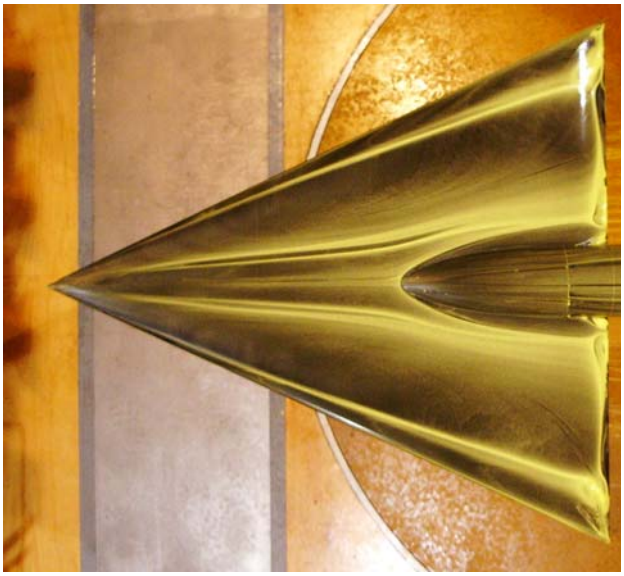

Fig. 26 Streamline visualisation using oil for rounded leading edge at $\alpha = 18^o$, $Re_{l_\mu} = 2 \cdot 10^6$ and $M = 0.14$.

As known from the pressure distributions, vortex breakdown occurs over the wing at $x/c_r =$ 0.85 for the rounded leading edge at an angle of attack of $\alpha = 23^o$ (Fig. 27), causing a kink in the secondary separation line. This behaviour is a sign for vortex breakdown, as the lateral positive pressure gradient downstream of breakdown becomes weaker compared to the fully developed case and, therefore, the secondary separation is closer to the leading edge.

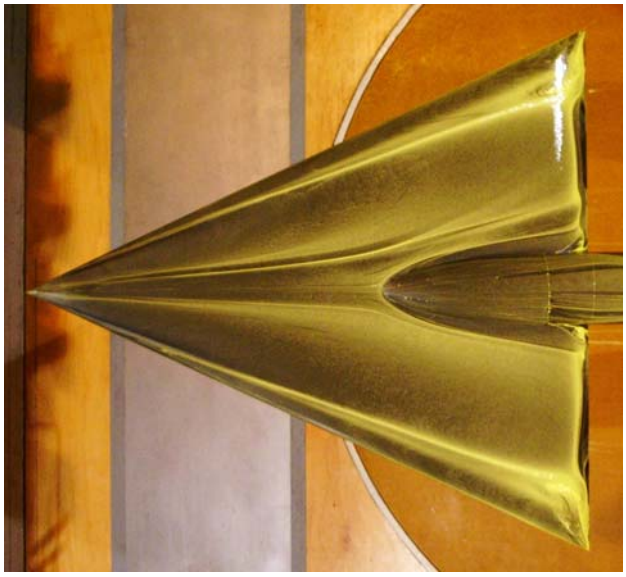

Fig. 27 Streamline visualisation using oil for rounded leading edge at $\alpha = 23^o$, $Re_{l_\mu} = 2 \cdot 10^6$ and $M = 0.14$.

At $\alpha = 13^o$ and $\alpha = 18^o$ (Fig. 25 and 26) two lines in the inboard area of the wing are visible. In the region of the apex the flow separates and is not able to follow the leading edge. Therefore, the separated flow is transported in freestream direction. The outer line is the separation line and the inner line the reattachment line of the vortex formed by this apex separation. The vortex rotates in the same direction as the leading edge vortex. This phenomenon is very sensitive to the flow and only visible at certain Reynolds numbers and in the medium angle of attack range. Further investigations of this phenomenon will be performed using Particle Image Velocimetry and advanced Hot–wire anemometry.

4 Conclusions

The experiments reported here are performed within the International Vortex Flow Experiment 2 (VFE–2) to set up a data base for validation of high fidelity computational methods. Standard and advanced test techniques are applied to determine surface and field quantities on a generic 65^o swept delta wing configuration including sharp and blunt leading–edges. The present tests are conducted in the low speed regime at Reynolds numbers based on the mean aerodynamic chord of $Re_{l\mu} = (1 \div 2) \cdot 10^6$. Typical vortex topologies are addressed which are determined by the angle of attack chosen, namely:

- leading edge vortex evolution at $\alpha = 13^o$.
- fully developed leading edge vortex at $\alpha = 18^o$.
- vortex breakdown over the wing at $\alpha = 23^o$.

To assess comparable test conditions, steady surface pressure distributions obtained by NASA serve as reference quantities. The results presented here show an excellent agreement with the reference values substantiating high quality of test section flow conditions, measurement accuracy and model geometry and instrumentation. Thus, a common basis is established for all other tests.

The results of the steady pressure distributions reflect the existence of the vortex flow types as expected by the chosen angles of attack. Significant differences between the results for the sharp and blunt leading–edge case are mainly present in the upstream part where the vortex evolution depends strongly on the boundary layer development in case of the blunt leading–edge. Oil flow visualisation and laser light sheet tests inform about separation and reattachment lines, vortex trajectories and vortex core sizes. Thus, the evolution and development of primary and secondary vortices is documented in detail. A special phenomenon detected here for the first time is the development of an apex vortex for the low and moderate angle–of–attack range. This vortex of considerable energy forms immediately at the apex and progresses downstream in the inboard region.

Distributions of rms surface pressures show peak values in the area of strong gradients of the mean flow quantities. Maximum *rms* levels are observed for the case of blunt leading–edge. The amplitude spectra of the surface pressure fluctuations depict broadband characteristics for low and moderate angles of attack. Some energy concentration is associated with the transition process where rms peak levels are found for the rounded leading–edge. At higher angles of attack, vortex bursting occurs over the wing and the breakdown flow causes a narrow–band concentration of turbulent energy linked to a helical mode instability. The corresponding dominant reduced frequency decreases with angle of attack and chordwise station as the wavelength of the unstable mode increases with the size of the burst vortex core.

The research work will be continued conducting flowfield and boundary layer measurements based on advanced hot–wire anemometry to obtain high resolution turbulence data. Stereo PIV surveys will help to address the most interesting regions for the hot–wire experiments. All data are collected in a unique data base which will be available for analysis and validation purposes.

Acknowledgment

The authors would like to thank the German Research Association (DFG) for supporting the investigations. Furthermore, we would like to thank the VFE–2 network for the good scientific co–operation.

References

[1] C. Breitsamter. *Turbulente Strömungsstrukturen an Flugzeugkonfigurationen mit Vorderkantenwirbeln*. Dissertation, Technische Universität München, Herbert Utz Verlag (ISBN 3–89675–201–4), 1997.

[2] C. Breitsamter. Experimentelle Untersuchung der instationären Feldgrößen und Oberflächen-

drücke bei wirbeldominierter abgelöster Strömung an einem Deltaflügel. In *DGLR–Jahrbuch*, pages 26–29, Bonn–Bad Godesberg, Germany, September, 1995.

[3] J. Chu and J. M. Luckring. *Experimental Surface Pressure Data Obtained on* 65° *Delta Wing Across Reynolds Number and Mach Number Ranges*. NASA–TM–4645, Volume 1–Sharp Leading Edge, 1996.

[4] J. Chu and J. M. Luckring. *Experimental Surface Pressure Data Obtained on* 65° *Delta Wing Across Reynolds Number and Mach Number Ranges*. NASA–TM–4645, Volume 3–Medium–Radius Leading Edge, 1996.

[5] A. Elsenaar, L. Hjelmberg, K.-A. Bütefisch, and W. J. Bannink. The international vortex flow experiment. *AGARD–CP–437*, pages 9–1 to 9–23, 1988.

[6] A. Furman and C. Breitsamter. Delta wing steady pressure investigations for sharp and rounded leading edges. In *14. DGLR–Fach–Symposium der STAB*, Bremen, Germany, 16. – 18. November, 2004.

[7] I. Gursul. Criteria for location of vortex breakdown over delta wings. *Technical note, Aeronautical Journal*, May, 1995.

[8] D. Hummel. On the vortex formation over a slender wing at large angles of incidence. *AGARD–CP–247*, pages 15–1 to 15–17, 1978.

[9] D. Hummel. Effects of boundary layer formation on the vortical flow above slender delta wing. In *Paper 30, RTO Symposium on Enhancement of NATO Military Flight Vehicle Performance by Management of Interacting Boundary Layer Transition and Separation*, Prague, Czech Republic, 4. – 7. October, 2004.

[10] D. Hummel and G. Redeker. A new vortex flow experiment for computer code validation. In *Paper 8, RTO Symposium on Advanced Flow Management*, Loen, Norway, 7. – 11. Mai, 2001.

[11] J. M. Luckrig. Reynolds number, compressibility, and leading-edge bluntness effects on delta–wing aerodynamics. In *ICAS–2004–4.1.4*, 24^{th} *Congress of the International Council of the Aeronautical Sciences*, Yokohama, Japan, 29. August – 3. September, 2004.

[12] H. C. Oelker. *Aerodynamische Untersuchungen an kurzgekoppelten Entenkonfigurationen bei symmetrischer Anströmung*. Dissertation, Technische Universität Braunschweig, ZLR–Forschungsbericht, 1990.

[13] W. H. Rae Jr and A. Pope. *Low–Speed Wind Tunnel Testing*. Second edition, John Wiley and Sons, 1984.

[14] B. Wagner, S. Hitzel, M. A. Schmatz, W. Schwarz, A. Hilgenstock, and S. Scherr. Status of CFD validation on the vortex flow experiment. *AGARD–CP–437*, pages 10–1 to 10–10, 1988.